Article scientifique    Article    2022        **Published version**    Open Access

- - - - - - - - - - - - - - - - - - - - - - - - - - - - - - - - - - - - - - - - -

# Dual-layer collimator for improved spatial resolution in SPECT with CZT camera: an analytical and Monte Carlo study

- - - - - - - - - - - - - - - - - - - - - - - - - - - - - - - - - - - - - - - - -

Boutaghane, Nasreddine; Hesse, Michel; Bouzid, Boualem; Zaidi, Habib; Jamar, François; Walrand, Stephan

# Physics in Medicine & Biology

**IPEM** Institute of Physics and Engineering in Medicine

**CrossMark**

**OPEN ACCESS**

**PAPER**

## Dual-layer collimator for improved spatial resolution in SPECT with CZT camera: an analytical and Monte Carlo study

Nasreddine Boutaghane[1], Michel Hesse[2], Boualem Bouzid[1], Habib Zaidi[3] ●, François Jamar[2] and Stephan Walrand[2]

[1] University of Sciences and Technology Houari Boumediene, Algiers, Algeria
[2] Université Catholique de Louvain, Brussels, Belgium
[3] University Hospital of Geneva, Geneva, Switzerland
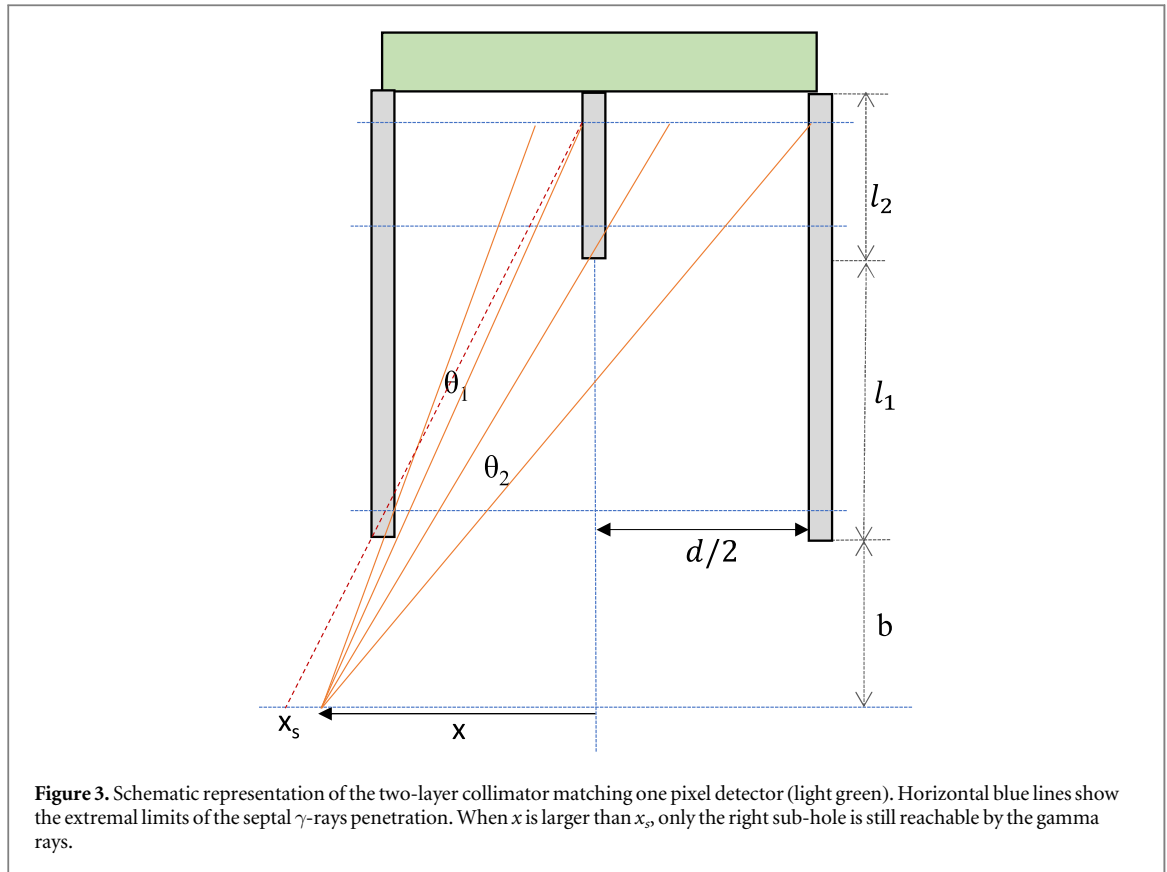
E-mail: nboutaghane83@yahoo.fr

## Abstract

*Purpose.* Current hole matching pixel detector (HMPD) collimators for SPECT imaging exist in two configurations: one hole per pixel (1HMPD) or four holes per pixel (4HMPD). The aim of this study was to assess the performance of a dual-layer collimator made by stacking up these two collimator types (1H/4HMDP) for low- and medium energy gamma emitters. *Method.* Analytical equations describing geometrical efficiency and full width at half maximum (FWHM) of the 1H/4HMDP collimator were derived. In addition, a fast dedicated Monte Carlo (MC) code neglecting scattering and designed for the collimator geometry was developed to assess the collimator's point spread function and to simulate planar and SPECT acquisitions. *Results.* A relative agreement between analytical equations and MC simulations better than 3% was observed for the efficiency and for the FWHM. The length of the two layers was optimized to get the best spatial resolution while keeping the geometrical efficiency equal to that of the 45 mm length 1HMPD collimator. An optimized combination of the 1H/4HMPD configuration with respective hole lengths of 20 and 13 mm has been derived. For source-collimator distances above 5 cm and equal collimator geometrical efficiency, the spatial resolution of this optimal 1H/4HMDP collimator supersedes that of the 45 mm length 1HMPD collimator, and that of the 19.1 mm length 4HMPD collimator. This improvement was observed in simulations of bar phantom planar images and of hot rods phantom SPECT. Remarkably, the spatial resolution was preserved along the whole radial range within the Jaszczak phantom. *Conclusion.* The 1H/4HMDP collimator is a promising solution for CZT SPECT imaging of low- and medium energy emitters.

## Introduction

Since the introduction of the first imaging SPECT camera invented by Anger (1958), different design trends have been developed using continuous and pixelated scintillation crystals (Garcia *et al* 2011, Gordon DePuey 2012). A number of constructors have focused on the design of SPECT cameras by optimizing collimators dedicated for the explored organs and for the energies of the used radionuclides. Therefore, to span all the possible radionuclides to image most organs, the exchange of collimators was as adopted along with the parallel-hole collimator, which was proposed since the first images acquire with Anger camera. Before designing this important component, analytical calculations and Monte Carlo modeling have been considered as an important tool to their optimization. Many analytical formulations have been developed for parallel-hole, converging and pinhole collimators (Tsuit and Gullberg 1990, Rentmeester *et al* 2007, Cherry *et al* 2012).

In the last two decades, the developments focused on the replacement of standard detectors-based scintillation crystals by new generations of solid-state pixelated CZT detectors (Park *et al* 2013). Compared to monolithic NaI-PMTs tandem, CZT detectors have a better energy resolution, are more robust, their performances are not altered by aging as such as for the PMTs and they do not require a large outer dead area.

**Figure 1.** Schematic representation of the two-layer collimator matching one pixel detector (light green). Horizontal blue lines show the extremal limits of the septal $\gamma$-rays penetration.

This last property allows setting several compact detectors close together according to a geometry which focuses on a narrow region of interest which increases the sensitivity on this region (Hutton 2010, Germano *et al* 2013). Nine swiveling vertical columns equipped with a one hole matching pixel detector (1HMPD) configuration has been developed by Spectrum Dynamics for the DSPECT system (Erlandsson *et al* 2009). GE Healthcare has designed the Discovery NM 530c system, which consists of 19 stationary small pixelated CZT detectors focused with 19 pinhole collimators (Slomka *et al* 2009, Garcia *et al* 2011). Both systems significantly improve the sensitivity in cardiac study (Gambhir *et al* 2009, Kennedy *et al* 2014).

Recently, large pixelated CZT cameras for general-purpose studies have been commercialized. This conceptual design will likely replace traditional large scintillation crystals-based design. To this end, the potential use of a large field-of view of pixelated CZT detector has recently been introduced by GE Healthcare through the design of the large field-of-view GE NM/CT 870 CZT camera for general-purpose clinical SPECT imaging with different parameter characteristics of the 1HMPD configuration (Ito *et al* 2021).

Spectrum dynamics introduced a new version of 360 degree CZT VERITON-CT system with a four holes matching pixel detector (4HMPD) configuration (Desmonts *et al* 2020). Recently, the full-ring enclosed system (GE StarGuide) has also been developed with the 4HMPD configuration (Serre *et al* 2021).

A previous study (Boutaghane *et al* 2019) has shown that the 4HMPD configuration improves spatial resolution and contrast. However, the use of this concept with medium energy emitters suffers from an increase in septal penetration fraction. We hypothesize that using a dual-layer collimator made by stacking a 1-hole and a 4-hole collimator together, both matching the detector pixelization, might be a solution to this problem.

The aim of this work was thus to assess intrinsic dual-layer collimators performance for low and medium energy emitters. To this end, analytical equations describing the geometrical efficiency and the collimators' spatial resolution were derived. In addition, a fast Monte Carlo (MC) code neglecting scattering and designed for the dual-layer collimator geometry was developed to assess the collimator's point spread function (PSF) shape and to simulate planar and SPECT acquisitions.

## Materials and methods

### Analytical geometric efficiency

Figure 1 shows a schematic representation of collimator hole cross-section in the *x*-axis direction. The septa penetration can be taken into account by assuming that the $\gamma$-rays can cross the septa within a distance $1/\mu$ to the septa edge (dashed horizontal blue lines) where $\mu$ is the attenuation of the septa material.

**Figure 2.** Schematic representation of the two-layer collimator matching one pixel detector (light green). Horizontal blue lines show the extremal limits of the septal $\gamma$-rays penetration.

Let's consider the right sub-hole, by choosing the $x$-axis origin at the inner side of the internal septa of thickness $s_i$, the intersection $x_m$ of the dashed red line crossing the two left penetration points on the effective top edge of the septa is given by:

$$x_m = (d + s_i)\frac{\widetilde{l_2}}{2\,l_1}\,,\tag{1}$$

where the $\sim$ operator is defined as:

$$\tilde{l} = 1 - 2/\mu \text{ if } l > 2/\mu = 0 \text{ otherwise}\tag{2}$$

when $x_m > (d - s_i)/2$ all the $\gamma$-rays coming from the left have to cross the internal septa to be detected. This condition can be re-written as:

$$\widetilde{l_2} \geqslant l_1 \frac{1 - s_i/d}{1 + s_i/d}\tag{3}$$

1st case: $\widetilde{l_2} \geqslant l_1 \frac{1 - s_i/d}{1 + s_i/d}$

Assuming $d/2 \ll l_2$ we get:

$$\theta_1 \approx \frac{x}{\widetilde{l_2}}\tag{4}$$

$$\theta_2 \approx \frac{(d - s_i)/2 - x}{\widetilde{l_1 + l_2}}.\tag{5}$$

The mean effective angular aperture of the right sub-hole is given by the integral:

$$\Theta = \frac{2}{d - s_i}\int_{(d-s_i)/2}^{0}\left(\frac{x}{\widetilde{l_2}} + \frac{(d - s_i)/2 - x}{\widetilde{l_1 + l_2}}\right)dx\tag{6}$$

which trivially gives:

$$\Theta = \frac{(d - s_i)/2}{2}\left(\frac{1}{\widetilde{l_1 + l_2}} + \frac{1}{\widetilde{l_2}}\right)\tag{7}$$

for a circular hole, the efficiency is just the solid angle (divided by $4\pi$) obtained by making a $2\pi$ revolution of the aperture $\Theta$, which in spherical coordinates is given by the double-integration:

$$\frac{1}{4\pi}\int_0^{2\pi}d\varphi\int_0^{\Theta/2}\sin\theta d\theta = \frac{1}{2}\left(1 - \cos\frac{\Theta}{2}\right) \approx \frac{\Theta^2}{16}.\tag{8}$$

For a square aperture equation (8) has to be multiplied by the square to inner circle area ratio, i.e. $4/\pi$, taking into account the sub-holes surface to detector surface ratio $((d - s_i)/2)^2/((d + s_e)/2)^2$, we have for the collimator efficiency:

**Figure 3.** Schematic representation of the two-layer collimator matching one pixel detector (light green). Horizontal blue lines show the extremal limits of the septal $\gamma$-rays penetration. When $x$ is larger than $x_s$, only the right sub-hole is still reachable by the gamma rays.

$$g = \frac{4}{\pi} \frac{((d-s_i)/2)^2}{((d+s_e)/2)^2} \frac{\Theta^2}{16} \tag{9}$$

resulting in the final expression:

$$g = \frac{1}{4\pi} \frac{1}{((d+s_e)/2)^2} \left( \frac{((d-s_i)/2)^2}{2} \left( \frac{1}{\widetilde{l_1+l_2}} + \frac{1}{\widetilde{l_2}} \right) \right)^2 \tag{10}$$

when $l_1 = 0$, equation (10) reduces to:

$$g = \frac{1}{4\pi} \frac{1}{((d+s_e)/2)^2} \left( \frac{((d-s_i)/2)^2}{\widetilde{l_2}} \right)^2 \tag{11}$$

which is the conventional geometric efficiency for a square hole collimator of hole inner size $(d-s_i)/2$ (Cherry *et al* 2012).

$\underline{2^{\text{nd}} \text{ case}}$: $\widetilde{l_2} \leqslant l_1 \frac{1-s_i/d}{1+s_i/d}$

Figure 2 shows that in this case the region $x < x_m$ corresponds to $\gamma$-rays never intersected by the left septa, while the region $x > x_m$ region corresponds to $\gamma$-rays never intersected by the internal septa.

The acceptance angles are given by:

$$\theta_1 \approx \frac{x}{\widetilde{l_2}} \tag{12}$$

$$\theta_2 \approx \frac{(d-s_i)/2 - x}{\widetilde{l_1+l_2}} \tag{13}$$

$$\theta \approx \frac{d}{\widetilde{l_1+l_2}} \tag{14}$$

we have:

$$\theta_1 + \theta_2 \approx \frac{1}{(\widetilde{l_1+l_2})} \left( x \frac{l_1}{\widetilde{l_2}} + (d-s_i)/2 \right). \tag{15}$$

The effective total angular aperture of the right sub-hole is given by the integral:

$$\Theta = \frac{1}{(\widehat{l_1 + l_2})}\left(\int_0^{(d+s_i)\frac{\widetilde{l_2}}{2\,l_1}}\left(x\,\frac{l_1}{\widetilde{l_2}} + (d - s_i)/2\right)dx + \int_{(d+s_i)\frac{\widetilde{l_2}}{2\,l_1}}^{(d-s_i)/2} d\ dx\right). \tag{16}$$

The trivial integration gives:

$$\Theta = \frac{1}{2(\widehat{l_1 + l_2})}\left(\frac{(d + s_i)^2}{4}\,\frac{\widetilde{l_2}}{l_1} + \frac{d^2 - s_i{}^2}{2}\,\frac{\widetilde{l_2}}{l_1} + d\left(d - s_i - (d + s_i)\frac{\widetilde{l_2}}{l_1}\right)\right). \tag{17}$$

Using equation (9) we get for the collimator efficiency:

$$g = \frac{1}{4\pi}\,\frac{1}{(d + s_e)^2}\,\frac{1}{(\widehat{l_1 + l_2})^2}\left(\frac{(d + s_i)^2}{4}\,\frac{\widetilde{l_2}}{l_1} + \frac{d^2 - s_i{}^2}{2}\,\frac{\widetilde{l_2}}{l_1} - d(d + s_i)\frac{\widetilde{l_2}}{l_1} + d(d - s_i)\right)^2. \tag{18}$$

When $l_2 = 0$ and $s_i = 0$ equation (18) reduces to:

$$g = \frac{1}{4\pi}\,\frac{d^2}{(d + s_e)^2}\,\frac{d^2}{(\widetilde{l_1})^2} \tag{19}$$

which is the conventional square hole collimator efficiency (Cherry *et al* 2012).

**Analytical spatial resolution**

The NEMA NU 1-2018 protocol for pixelated detector (NEMA) was used for the spatial resolution computation. Analytically this spatial resolution is twice the source shift needed to reduce by twofold the intensity in the pixel detector on which the source was initially centered (Siman and Kappadath 2012). Figure 3 shows the two acceptance angles $\Theta_i$ for a point source shifted by the distance $x$ from the detector pixel center, note that in this computation it is no longer needed to differentiate the two cases.

The two acceptance angles can be written as the differences of the angles versus the left dashed black line, i.e.:

$$\theta_1(x) \approx \max\left(\frac{x - s_i/2}{b + l_1 + l_2 - 1/\mu} - \frac{x - d/2}{b + 1/\mu}, 0\right)\text{if } x > d/2$$

$$\approx \frac{d/2 - s_i/2}{b + l_1 + l_2 - 1/\mu}\text{otherwise} \tag{20}$$

$$\theta_2(x) \approx \max\left(\frac{x + d/2}{b + l_1 + l_2 - 1/\mu} - \frac{x + s_i/2}{b + l_1 + 1/\mu}, 0\right) \tag{21}$$

the PSF is given by:

$$\text{PSF}(x) \approx \theta_1(x) + \theta_2(x) \tag{22}$$

and the FWHM is by:

$$\text{PSF}\left(\frac{\text{FWHM}}{2}\right) = \frac{1}{2}\frac{d - s_i}{b + l_1 + l_2 - 1/\mu} \tag{23}$$

the right term of equation (23) being the PSF value when the source is centered in front of the hole.

A trivial calculation gives:

$$\text{FWHM} = \left(\frac{d}{b + 1/\mu} - \frac{s_i}{b + l_1 + 1/\mu}\right)\Big/\left(\frac{1}{b + 1/\mu} + \frac{1}{b + l_1 + 1/\mu} - \frac{2}{b + l_1 + l_2 - 1/\mu}\right). \tag{24}$$

**Monte Carlo code**

A fast Monte Carlo code modelling the dual-layer collimators coupled to an ideal pixelated detector was developed in visual c++. SIMD oriented fast Mersen twister random generators were used for uniform random drawing (Saito and Matsumonto). Scattering was neglected, and the probability of a $\gamma$-ray to cross any septa was given by $e^{-\mu l}$ where $\mu$ is the septa material attenuation coefficient and $l$ the crossing length within the septa. Beside neglecting the scattering process, the simulation speed is also significantly improved by the fact that the computation of the crossing point of the $\gamma$-rays with the collimator septa directly take into account that the septa are periodically set in the two transverse directions.

In order to evaluate the impact of neglecting the scattering, one collimator PSF was also computed using GATE 8.2 (Sarrut *et al* 2014) for an ideal pixelated detector, i.e. the gamma ray energy was forced to be totally
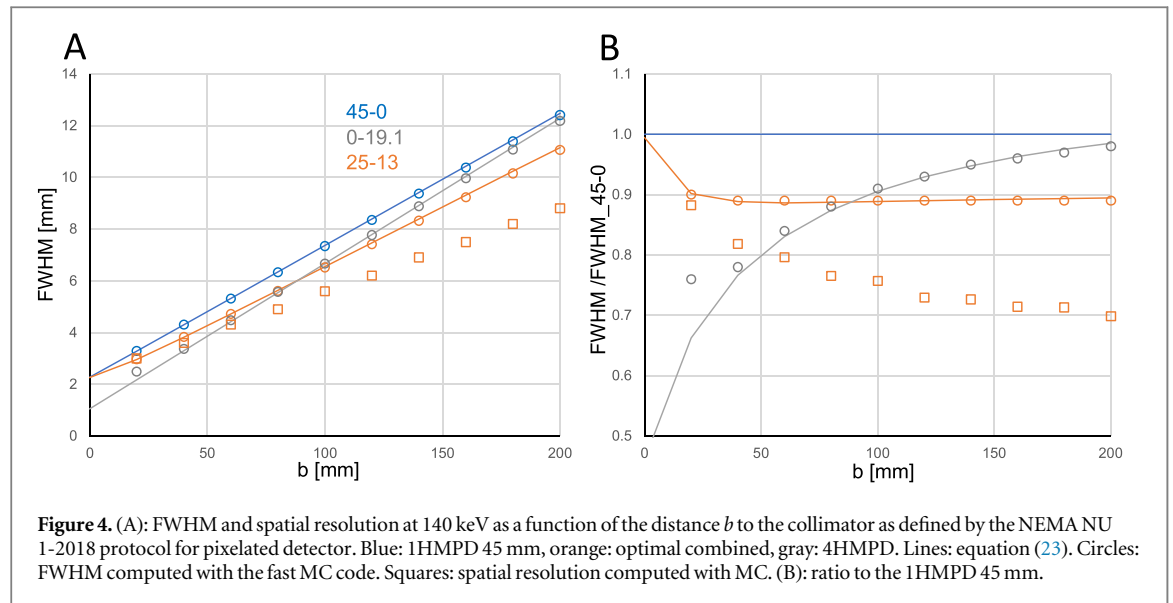
**Figure 4.** (A): FWHM and spatial resolution at 140 keV as a function of the distance $b$ to the collimator as defined by the NEMA NU 1-2018 protocol for pixelated detector. Blue: 1HMPD 45 mm, orange: optimal combined, gray: 4HMPD. Lines: equation (23). Circles: FWHM computed with the fast MC code. Squares: spatial resolution computed with MC. (B): ratio to the 1HMPD 45 mm.

**Table 1.** Analytical and fast MC code comparison of geometric efficiencies $g$ and FWHM for dual-layer collimators, the layers thickness $l_1$ and $l_2$ of which were chosen to get $g = 1.71 \times 10^{-4}$ using the fast MC code.

| $l_1$–$l_2$ [mm] | 45–0.0 | 40–1.2 | 35–4.8 | 30–7.9 | 25–10.7 | 20–13.0 | 15–14.2 | 10–15.3 | 5–17.0 | 0–19.1 |
|---|---|---|---|---|---|---|---|---|---|---|
| $g \times 10^4$ (equations (10) or (18)) | 1.75 | 1.76 | 1.76 | 1.78 | 1.78 | 1.77 | 1.77 | 1.77 | 1.74 | 1.74 |
| FWHM (MC) [mm] | 7.34 | 7.26 | 6.93 | 6.75 | 6.59 | 6.52 | 6.66 | 6.84 | 6.84 | 6.67 |
| FWHM (equation (23)) [mm] | 7.37 | 7.32 | 7.00 | 6.80 | 6.63 | 6.55 | 6.69 | 6.87 | 6.85 | 6.67 |

depose when it hits the detector. By the way, the only physical difference between the fast MC code and GATE simulations was the absence of scattering within the collimator septa.

### Dual layer optimization

The collimator reference was the WEHR lead collimator equipping the GE NM/CT 870 CZT camera, i.e. $\mu = 2.7$ and $0.71$ mm$^{-1}$ for 140 and 245 keV $\gamma$-rays, respectively. Other parameters were: detector pixel width $= 2.46$ mm, septal thickness $s_e = 0.2$ mm, collimator thickness $l_1 = 45$ mm ($l_2 = 0$), resulting in $g = 1.75$E-4 using equation (19).

The layer thickness $l_2$ was computed as a function of the decreasing $l_1$ thickness in order to keep the geometric efficiency computed by MC equal to that of the WEHR collimator. Afterwards the geometric efficiency was computed using equations (10) or (18), and the FWHM of the PSF was assessed with the fast MC code according to the NEMA NU 1-2018 protocol and also computed using equation (24). Additionally, the spatial resolution was also assessed as the minimal distance between 2 point-sources to distinguish a valley between the 2 point-sources in the intensity profile simulated using the fast MC code according to the NEMA NU 1-2018 protocol.

### Imaging evaluation

A high statistics bar phantom acquisition in whole-body mode was simulated with the fast MC code for a distance of 10 cm to the collimator. Whole-body mode acquisition was chosen because it corresponds to the NEMA NU 1-2018 protocol PSF assessment for pixelated detector. Also, the spatial resolution for pixelated detector is not uniform in static planar acquisition and locally depends on the transverse distance between activity transition and detector pixel edge position. For bar phantoms this results in moire effect (Kim *et al* 2018).

A high statistics SPECT acquisition of the Ultra deluxe Jaszczak hot rods insert was also simulated with the fast MC code, the rods inner diameter being 3.2, 4.8, 6.4, 7.9, 9.5 and 11.1 mm with a 5 cm length. The rotation radius was 20 cm, giving rods distances to the collimator ranging from 10 to 19 cm. This distance range is typically met in clinical SPECT imaging. The aim being to evaluate the intrinsic collimators performances, no attenuation and no scattering was applied within the phantom, and the acquisitions were reconstructed with the FBP algorithm of the MIM software 7.1.3 (Cleaveland, OH) in a $256 \times 256$ matrix (pixel size $= 1.23$ mm) from 256 simulated angle positions.
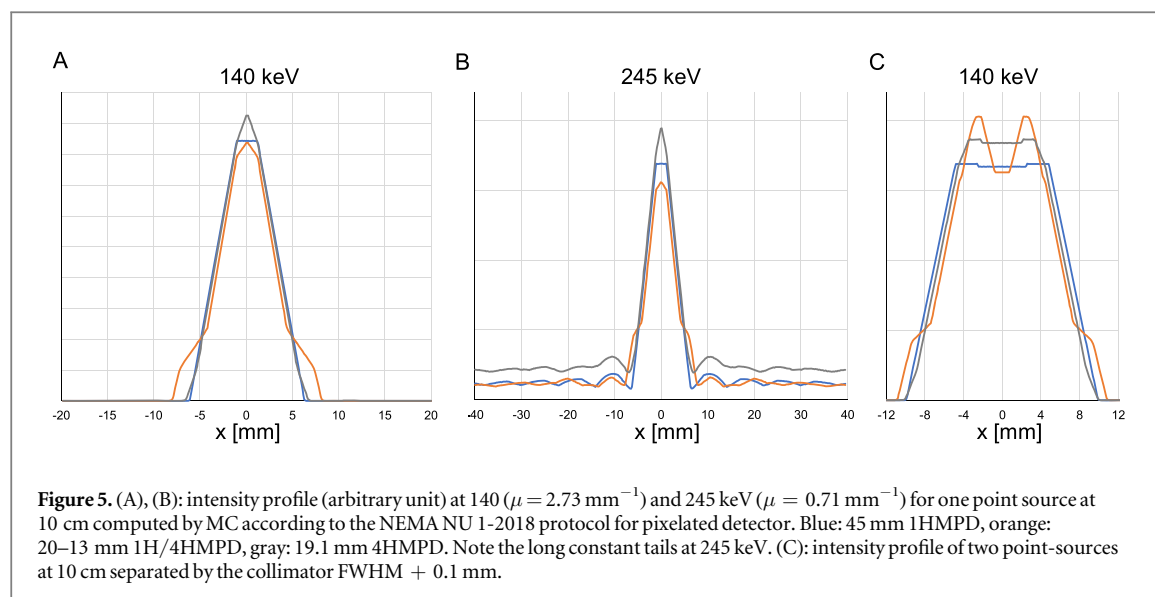
**Figure 5.** (A), (B): intensity profile (arbitrary unit) at 140 ($\mu = 2.73$ mm$^{-1}$) and 245 keV ($\mu = 0.71$ mm$^{-1}$) for one point source at 10 cm computed by MC according to the NEMA NU 1-2018 protocol for pixelated detector. Blue: 45 mm 1HMPD, orange: 20–13 mm 1H/4HMPD, gray: 19.1 mm 4HMPD. Note the long constant tails at 245 keV. (C): intensity profile of two point-sources at 10 cm separated by the collimator FWHM + 0.1 mm.

**Table 2.** FWHM of the different dual-layer collimators (coll.) of table 1 as a function of the distance (dist.) computed with the fast MC code and according to the NEMA NU 1-2018 protocol for pixelated detector (All numbers in table are in mm. Cells are colored in rainbow scale, i.e. for each row, green to red for FWHM ranging from the minimum to the maximum value of the row.)

| dist./coll. | 45-0.0 | 40-1.2 | 35-4.8 | 30-7.9 | 25-10.7 | 20-13.0 | 15-14.2 | 10-15.3 | 5-17.0 | 0-19.1 |
|---|---|---|---|---|---|---|---|---|---|---|
| 2 | 3.29 | 3.35 | 3.19 | 3.13 | 3.05 | 2.97 | 2.91 | 2.82 | 2.61 | 2.49 |
| 4 | 4.3 | 4.32 | 4.12 | 4.02 | 3.92 | 3.83 | 3.82 | 3.79 | 3.64 | 3.37 |
| 6 | 5.31 | 5.3 | 5.06 | 4.92 | 4.8 | 4.72 | 4.76 | 4.8 | 4.7 | 4.47 |
| 8 | 6.33 | 6.28 | 5.99 | 5.83 | 5.68 | 5.61 | 5.7 | 5.82 | 5.76 | 5.57 |
| 10 | 7.34 | 7.26 | 6.93 | 6.75 | 6.59 | 6.52 | 6.66 | 6.84 | 6.84 | 6.67 |
| 12 | 8.35 | 8.24 | 7.87 | 7.66 | 7.48 | 7.41 | 7.62 | 7.86 | 7.91 | 7.77 |
| 14 | 9.37 | 9.24 | 8.81 | 8.57 | 8.38 | 8.32 | 8.57 | 8.9 | 8.97 | 8.88 |
| 16 | 10.38 | 10.22 | 9.74 | 9.49 | 9.28 | 9.23 | 9.53 | 9.92 | 10.05 | 9.97 |
| 18 | 11.39 | 11.21 | 10.68 | 10.39 | 10.18 | 10.15 | 10.51 | 10.96 | 11.12 | 11.08 |
| 20 | 12.41 | 12.2 | 11.62 | 11.32 | 11.09 | 11.06 | 11.47 | 11.98 | 12.21 | 12.18 |

# Results

Table 1 shows the comparison between the analytical equation and the MC simulation for the collimator efficiencies and FWHM. The equations provided a relative overestimation of 2.9 $\pm$ 0.8% for the efficiency, while the FWHM agreement was better than 1%.

The color scaled table 2 shows the FWHM of the dual-layer collimator PSF as a function of the distance to the collimator computed with Monte Carlo according to the NEMA NU 1-2018 protocol for pixelated detector. The 20–13 collimator was chosen as optimal configuration.

Figure 4 shows the collimators FWHM (circles) and spatial resolution (rectangles) as a function of the source-collimator distance *b* for the three collimators configurations types (1HMPD, optimal 1H/4HMPD and 4HMPD) for 140 keV $\gamma$-rays. Spatial resolution was found equal to the FWHM for the mono-layer 1HMPD and 4HMPD collimators, but not for dual-layer 1H/4HMPD collimators.

Figures 5(A), (B) show the intensity profile at 140 and 245 keV for a point source at 10 cm computed by MC according to NEMA NU 1-2018 protocol for pixelated detector. All collimators exhibit constant long tails at 245 keV, especially the 4HMPD collimator the tails of which being twice that of the two other ones. The optimal dual-layer collimator PSF exhibits a narrow shoulder below 30% of the peak value. We will come back on this apparent drawback in the discussion section.

Figure 5(C) shows the intensity profile at 140 keV for 2 point-sources at 10 cm and separated by the collimator FWHM + 0.1 mm, i.e. 7.34, 6.52 and 6.67 mm (see table 2). Note that the valley between the two source peaks is much deeper for the optimal 1H/4HMPD collimator. In fact, the optimal collimator gives the
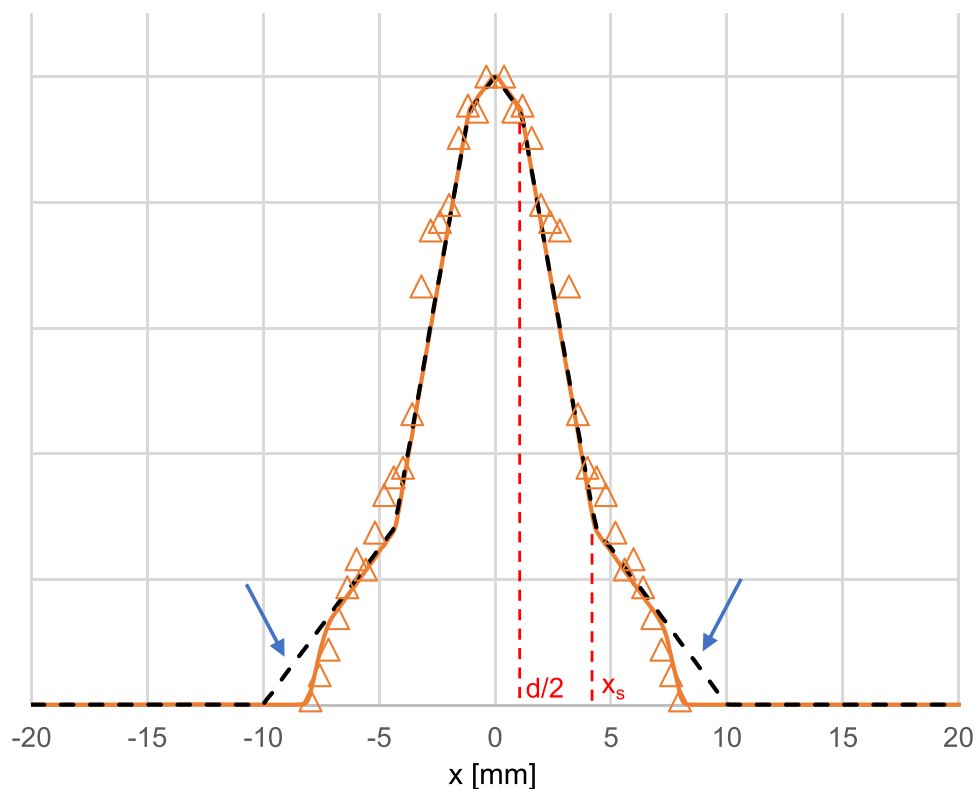
**Figure 6.** PSF at 140 keV of the collimator 20–13, computed with the fast MC code (orange curve), with GATE (orange triangles) and with the analytical equation (22) (black dashed curve). Note the wrong tail prolongations of the analytical PSF (blue arrows).
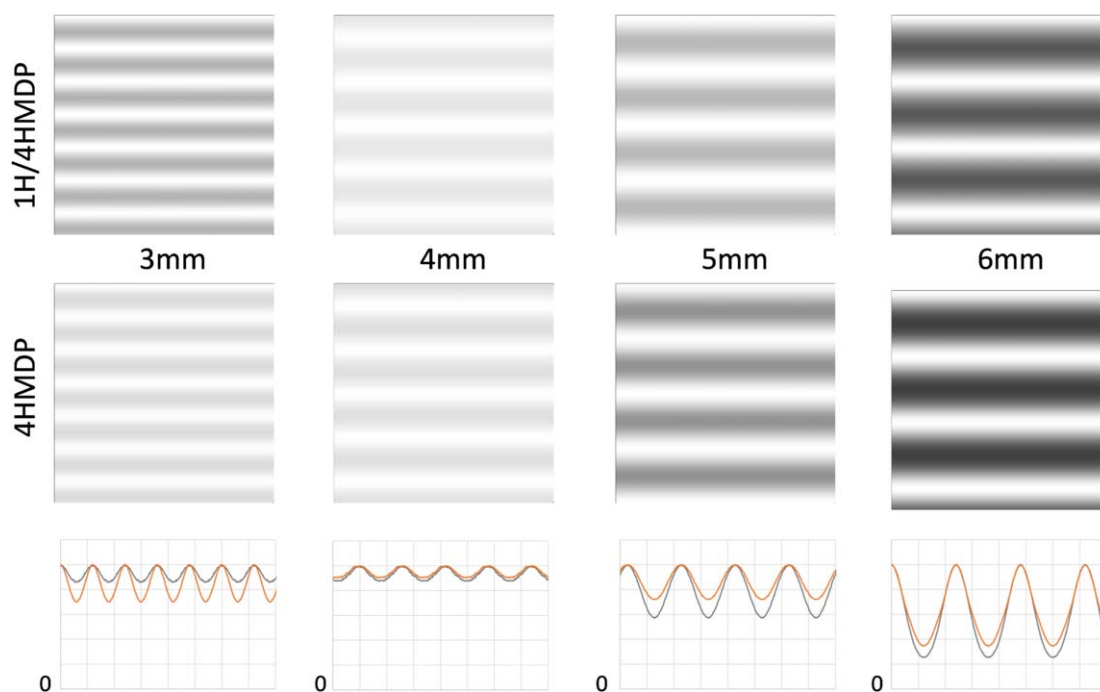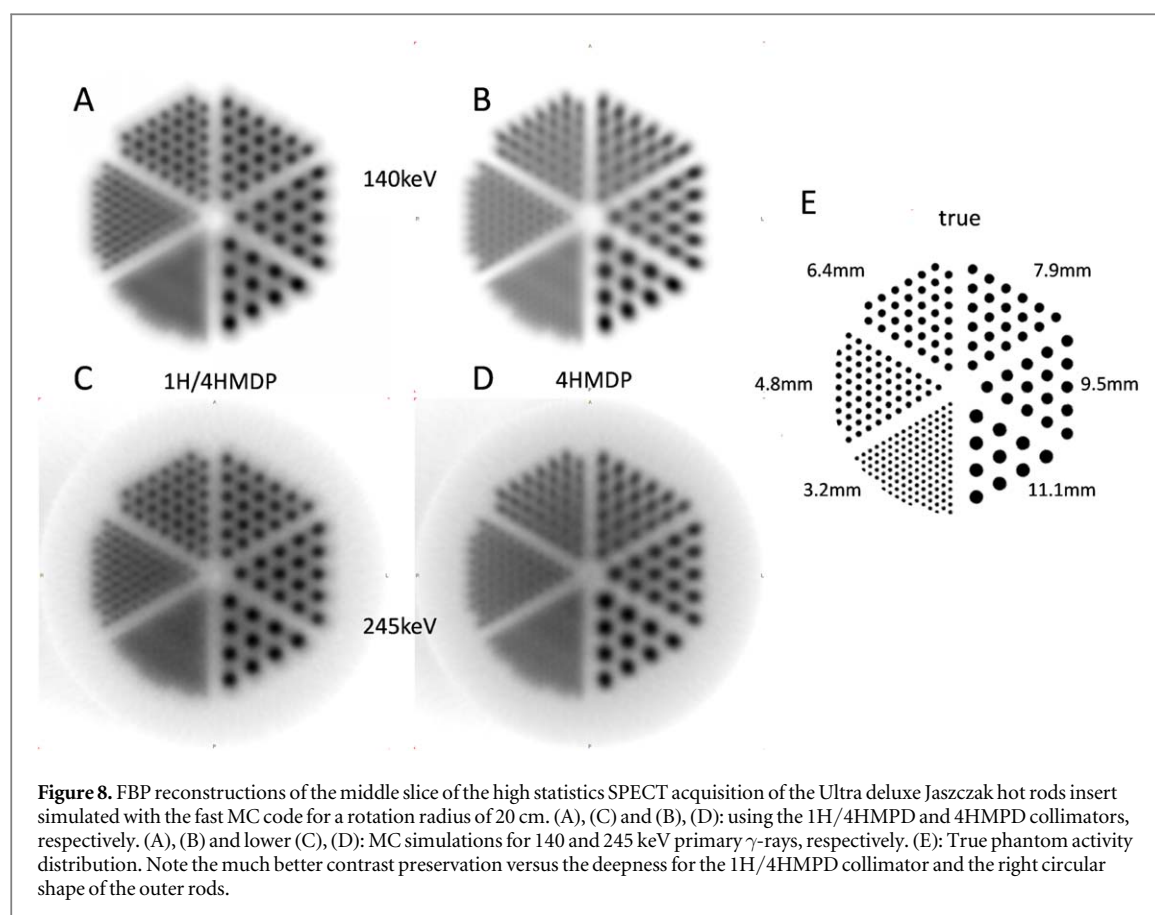


**Figure 7.** High statistics MC simulation of bar phantoms acquired in whole-body mode. Orange and grey curves: 1H/4HMPD and 4HMPD vertical profiles, respectively. Note the better contrast and valley deepness obtained by the 1H/4HMPD collimator for the 3 mm bar phantom. (The bar contrast of the 3–4 mm bar phantoms is so low that for some monitor tunings the grey bars can be invisible.)

**Figure 8.** FBP reconstructions of the middle slice of the high statistics SPECT acquisition of the Ultra deluxe Jaszczak hot rods insert simulated with the fast MC code for a rotation radius of 20 cm. (A), (C) and (B), (D): using the 1H/4HMPD and 4HMPD collimators, respectively. (A), (B) and lower (C), (D): MC simulations for 140 and 245 keV primary $\gamma$-rays, respectively. (E): True phantom activity distribution. Note the much better contrast preservation versus the deepness for the 1H/4HMPD collimator and the right circular shape of the outer rods.

same valley deepness than the two other ones for a shift of only 5.5 mm which can be considered as the actual spatial resolution of this collimator.

Figure 6 shows the PSF of the collimator 20–13 mm 1H/4HMPD computed with the fast MC code, with GATE and with the analytical equation (22). The artefactual tail prolongations of the analytical PSF result from the fact that equations (20)–(21) do not take into account the gamma ray absorption by the remote septa of the neighbor holes.

Figure 7 shows the MC simulation of whole-body mode acquisitions of bar phantoms located 10 cm far away from the collimator.

Figure 8 shows FBP reconstructed slices of the high statistics SPECT acquisition of the Ultra deluxe Jaszczak hot rods insert simulated by the fast MC code.

## Discussion

The study showed a relative agreement between the analytical equations and the MC simulations better than 3% and 1% for the efficiency and the FWHM, respectively (table 1). This agreement is a mutual cross-validation of the fast MC code and of the analytical equations. Furthermore, in the limit of the single layer collimator, these equations rightly reduce to the conventional efficiency and FWHM ones.

The results showed that for an equal efficiency, the optimal 1H/4HMPD collimator provided: (1) a better spatial resolution than the 1HMPD one (figure 4); (2) a better spatial resolution than the 4HMPD one for distances above 5 cm that are typically met in clinical SPECT imaging (figure 4); (3) long constant tails at 245 keV twice lower than those observed with the 4HMPD collimator (figure 5C); (4) a deeper profile valley for two sources separated by the collimator FWHM (figure 5(B)).

The spatial resolution is the minimal distance between 2 point-sources needed to distinguish 2 peaks in the intensity profile crossing the 2 sources. The spatial resolution is commonly assimilated to the FWHM of the PSF. In fact, this equality is only exact for triangular PSF which gives a constant intensity profile between 2 point-sources separated by the FWHM. However, this approximation is quite accurate for Gaussian shaped PSF.

The PSF of the 1H/4HMPD collimator computed with the fast MC code and with the equation (22) exhibits a shoulder on the low region confirmed by the GATE simulation (figure 5(A)). The shoulder result from the fact that when $|x| > |x_s|$ (see figures 3, 6) the intensity reduction is only due to the increasing of the inner septum

shadow which results in a twofold reduction of the PSF slope versus the region $|x| < |x_s|$ where the two septa shadows simultaneously increase. Afterwards, the absorption of the gamma rays by the remote septa of the neighbor hole dumps the PSF, an effect which is not taken into account by equations (20)–(21).

When the distance between two sources is smaller than the FWHM, the shoulder of one source is added to the peak position of the other one, and reciprocally. As a result, the valley deepness is increased (figure 5(B)). For this, it is mandatory for best spatial resolution evaluation to use another alternative of the isolated punctual source as well as the bar and Jaszczak phantoms. Figures 7–8 show that this feature improves the visualization of pattern scale lower than the FWHM, but at the cost of a little bit lower contrast for pattern scale larger than the FWHM. Remarkably, figure 8 shows that the contrast using the 1H/4HMPD is well preserved when moving away from the collimator. This better spatial resolution uniformity results in a better reproduction of the circular shape of the outer rods. These two benefits hold for 245 keV $\gamma$-rays.

This amazing benefit of having a shoulder in the PSF is a paradigm shift. Indeed, it is commonly accepted that faster is the PSF decrease, better is the spatial resolution. In contrary, the present simulations show that a narrow shoulder can improve the spatial resolution. Despite an extensive literature search among collimator or optical lenses studies, we did not find any other works describing this effect. Theoretical and simulation studies to determine the optimal shoulder shape will be valuable. However, the design and building of the collimator enabling the optimal PSF shape could be highly challenging and even impossible.

Our study has the limitation of neglecting the intra-septa scattering. This choice was justified by the intent to cross validate the fast MC code with analytical equations in which septa scattering cannot be modelized. Another reason was to obtain a fast MC code allowing fast SPECT simulation in order to make easier a first optimization of the collimator parameters. Last, the GATE simulation of the PSF which included intra-septa scattering is very similar to that obtained with the fast MC code.

Obviously, real CZT-1H/4HMDP performance will be hampered by statistical noise and intra phantom or patient attenuation and scattering. However, this preliminary study was to evaluate the intrinsic collimator performances. These intrinsic performances will still have to be evaluate in non-conventional SPECT samplings such as performed in the GE StarGuide (Serre *et al* 2021) and in the Spectrum-Dynamics VERITON-CT (Desmonts *et al* 2020) system.

Further realistic SPECT acquisition using full-physics MC code will have to be performed.

## Conclusion

For source-collimator distance above 5 cm and equal geometrical collimator efficiency, the spatial resolution of the optimal 1H/4HMDP collimator supersede that of the 45 mm length 1HMPD collimator, as well as that of the 19.1 mm length 4HMPD collimator. This improvement was observed in simulated bar phantom planar imaging and in hot rods phantom SPECT. Remarkably, the spatial resolution was preserved on the whole deepness of the Jaszczak phantom. The newly proposed combined collimator was investigated to be another solution to the existing parallel-hole collimators for large field of view pixelated CZT detector and full-ring enclosed detector for low and medium energy emitters.

## ORCID iDs

Habib Zaidi ⓘ https://orcid.org/0000-0001-7559-5297

## References

Anger H O 1958 Scintillation camera *Rev. Sci. Instrum.* **29** 27–33

Boutaghane N, Bouzid B and Zaidi H 2019 Conceptual design of a large pixelated CZT detector with four-hole collimator matched pixel detector for SPECT imaging: a Monte Carlo simulation study *J. Instrum.* **14** P02026–02026

Cherry S R, Sorenson J A and Phelps M E 2012 *Physics in Nuclear Medicine E-Book* (Philadelphia, PA: Elsevier Health Sciences) (https://elsevier.com/books/physics-in-nuclear-medicine/cherry/978-1-4160-5198-5)

Desmonts C, Bouthiba M A, Enilorac B, Nganoa C, Agostini D and Aide N 2020 Evaluation of a new multipurpose whole-body CzT-based camera: comparison with a dual-head anger camera and first clinical images *EJNMMI Phys.* **7** 17

Erlandsson K, Kacperski K, Van Gramberg D and Hutton B F 2009 Performance evaluation of D-SPECT: a novel SPECT system for nuclear cardiology *Phys. Med. Biol.* **54** 2635–49

Gambhir S S *et al* 2009 A novel high-sensitivity rapid-acquisition single-photon cardiac imaging camera *J. Nucl. Med.* **50** 8

Garcia E V, Faber T L and Esteves F P 2011 Cardiac dedicated ultrafast SPECT cameras: new designs and clinical implications *J. Nucl. Med.* **52** 210–7

Germano G, Slomka P J and Berman D S 2013 New hardware solutions for cardiac SPECT Imaging *Curr. Cardiovascular Imaging Rep.* **6** 305–13

Gordon DePuey E 2012 Advances in SPECT camera software and hardware: currently available and new on the horizon *J. Nucl. Cardiol.* **16** 551–81

Hutton B F 2010 'New SPECT technology: potential and challenges *Eur. J. Nucl. Med. Mol. Imaging* **37** 1883–6

Ito T *et al* 2021 Experimental evaluation of the GE NM/CT 870 CZT clinical SPECT system equipped with WEHR and MEHRS collimator *J. Appl. Clin. Med. Phys.* **22** 165–77

Kennedy J A, Israel O and Frenkel A 2014 3D iteratively reconstructed spatial resolution map and sensitivity characterization of a dedicated cardiac SPECT camera *J. Nucl. Cardiol.* **21** 443–52

Kim J, Kim S-K and Saveljev V 2018 Moiré effect in displays: a tutorial *Opt. Eng.* **57** 030803

NEMA NEMA NU 1-2018 (https://techstreet.com/nema/standards/nema-nu-1-2018?gateway_code=nema&product_id=2073744)

Park M A, Moore S C, Muller S P, McQuaid S J and Kijewski M F 2013 Performance of a high-sensitivity dedicated cardiac SPECT scanner for striatal uptake quantification in the brain based on analysis of projection data *Med. Phys.* **40** 042504

Rentmeester M C, van der Have F and Beekman F J 2007 Optimizing multi-pinhole SPECT geometries using an analytical model *Phys. Med. Biol.* **52** 2567–81

Saito M and Matsumonto M SIMD-oriented fast mersenne twister (SFMT): twice faster than mersenne twister (http://math.sci.hiroshima-u.ac.jp/~m-mat/MT/SFMT/index.html)

Sarrut D *et al* 2014 A review of the use and potential of the GATE Monte Carlo simulation code for radiation therapy and dosimetry applications *Med. Phys.* **41** 064301

Serre D *et al* 2021 Apport des caméras CZT grand champ 2D et 3D dans l'évolution des pratiques cliniques *Méd. Nucl.* **45** 234–9

Siman W and Kappadath S C 2012 Performance characteristics of a new pixelated portable gamma camera *Med. Phys.* **39** 3435–44

Slomka P J, Patton J A, Berman D S and Germano G 2009 Advances in technical aspects of myocardial perfusion SPECT imaging *J. Nucl. Cardiol.* **16** 255–76

Tsuit B M W and Gullberg G T 1990 The geometric transfer function for cone and fan beam collimators *Phys. Med. Biol.* **35** 87